Available online at www.sciencedirect.com
ScienceDirect
Trans. Nonferrous Met. Soc. China 31(2021) 2716−2728
Transactions of Nonferrous Metals Society of China
www.tnmsc.cn

Microstructure, microhardness and corrosion resistance of laser cladding Ni−WC coating on AlSi5Cu1Mg alloy

Min ZENG[1,2,3], Hong YAN[1,2], Bao-biao YU[1], Zhi HU[1]

1. School of Mechanical and Electrical Engineering, Nanchang University, Nanchang 330031, China;
2. Nanchang Key Laboratory of Light Alloy Preparation & Processing, Nanchang 330031, China;
3. School of New Energy Vehicles, Nanchang Institute of Science & Technology, Nanchang 330108, China

Received 30 October 2020; accepted 28 April 2021

Abstract: The microstructure, microhardness, and corrosion resistance of laser cladding Ni−WC coating on the surface of AlSi5Cu1Mg alloy were investigated by scanning electron microscopy, X-ray diffraction, microhardness testing, immersion corrosion testing, and electrochemical measurement. The results show that a smooth coating containing NiAl, Ni_3Al, M_7C_3, $M_{23}C_6$ phases (M=Ni, Al, Cr, W, Fe) and WC particles is prepared by laser cladding. Under a laser scanning speed of 120 mm/min, the microhardness of the cladding coating is 9−11 times that of AlSi5Cu1Mg, due to the synergistic effect of excellent metallurgical bond and newly formed carbides. The Ni−WC coating shows higher corrosion potential (−318.09 mV) and lower corrosion current density (12.33 μA/cm^2) compared with the matrix. The crack-free, dense cladding coating obviously inhibits the penetration of Cl^- and H^+, leading to the remarkedly improved corrosion resistance of cladding coating.

Key words: laser cladding; Ni−WC coating; AlSi5Cu1Mg; mechanical properties; corrosion resistance

1 Introduction

Aluminum alloy with remarkable metallurgical properties such as high specific strength, forming quality, and thermal conductivity is considered as a promising lightweight structural material widely used in manufacturing, transportation, and spaceflight areas [1,2]. However, the inferior corrosion and wear resistances of aluminum alloys are major challenges hindering large-scale implementation in harsh environments. To obtain outstanding corrosion and wear resistance of aluminum alloys, a method was developed to prepare metal matrix composite coating on the surface by various surface modification techniques, such as electroplating [3], thermal spraying [4], plasma spraying [5], arc welding [6], and laser cladding [7]. It is worth mentioning that laser cladding possesses features of good metallurgical bonding, low dilution ratio, and a compact microstructure and has received abundant interest in the past few years [8−10].

In laser cladding technology, the design of the metal matrix composite powder is of vital importance to control and minimize wear and corrosion behavior. The hard phases, such as SiC [11], WC [12], TiC [13] and Cr_3C_2 [14] particles, were employed in the aggressive environments. Compared to other carbides, WC particles have high hardness, high density, and good wettability with the bonding metal, which is more suitable for enhancing the performance of the coating [15]. HU et al [16] successfully deposited WC−12Co composite coating with no porosity, cracks, or deficiencies such as decarburization on the 304 stainless steel substrate by laser cladding, which showed high microhardness and low friction

Corresponding author: Hong YAN, Tel: +86-791-83969622, E-mail: hyan@ncu.edu.cn
DOI: 10.1016/S1003-6326(21)65687-X

coefficient. A series of studies have indicated that the addition of WC to the metal binder can lead to good comprehensive properties with high wear resistance [17−20]. However, the relatively poor corrosion resistance of WC reinforced metal-based composite coating limits its applications.

Under the premise of maintaining wear resistance, it is necessary to improve corrosion resistance. The choice of metal matrix is also critical. Among various metallic matrix materials, Ni-based alloys containing B and Si elements have the feature of ‘‘self-fluxing’’, which can reduce the liquidus temperature, cause the precipitation of hard particles during laser cladding, and exhibit outstanding corrosion resistance properties [21]. SCHOLL et al [22] evaluated the corrosion behavior of Co+10vol.%WC, Ni+10vol.%WC, and Fe+10vol.%WC coatings in sulfuric acid solution. The relative corrosion resistance was established as (WC, Ni) > (WC, Co) > (WC, Fe), confirming the Ni+WC coating displayed the best corrosion resistance. CHO et al [23] compared the corrosion behavior of the high velocity oxygen fuel-sprayed WC−Co, WC−Co−Cr, WC−CrC−Ni and WC−Ni composite coatings in 5 wt.% H_2SO_4 solution. The WC−CrC−Ni coating with fine micromorphology and few cracks presented the best corrosion resistance. HIDOUCI et al [24] compared the microstructure and mechanical properties of laser cladding WC coatings with Ni-based and Co-based binders. The Ni-based coating has a dense structure and high oxidation resistance, which is suitable for corrosion. FARAHMAND et al [25] investigated the corrosion behavior of a Ni−WC coating modified by adding nano-WC, La_2O_3 and Mo. It has been observed that the better corrosion behavior was due to an optimal addition of nano-WC (5 wt.%), La_2O_3 (1 wt.%), and Mo (1 wt.%), which can refine the grain size of the Ni binder and improve the passivation capability of the coating.

At present, most research was focused on the preparation of a WC/Ni-based layer on the steel surface, while research on the preparation of WC/Ni-based coatings on the surface of aluminum alloys is less. Furthermore, the primary purpose of adding WC particles is to improve the wear resistance, where less attention has been paid to their effect on corrosion resistance. In this work, the Ni−WC coating was fabricated by laser cladding and the microstructure, microhardness, and corrosion resistance of the cladding coating were systematically investigated. Moreover, the corrosion mechanism of cladding coating was discussed. This work can provide a theoretical basis for surface modification and application of aluminum alloys.

2 Experimental

2.1 Materials

An AlSi5Cu1Mg alloy was used as the substrate for the laser cladding experiment, and its chemical composition is given in Table 1. The sample should be cut into a slice with the size of 100 mm × 50 mm × 12 mm, polished with sand-paper, and cleaned with ethanol for 15 min to remove the surface oxide layer.

Table 1 Chemical composition of AlSi5Cu1Mg (wt.%)

Al	Si	Cu	Mg	Fe	Mn	Zn
Bal.	4.5	1.0	0.4	0.5	0.5	0.3

Ni60+20wt.%WC composite powder was used as the cladding material for layer cladding. The chemical composition of Ni60 alloy powder with a particle size of 20−50 μm and a melting point of 960−1040 °C is given in Table 2. 20 wt.% WC powder with a particle size of 20−80 μm was added into the Ni60 alloy power and ball mill mixing for 20 min produced Ni60+20wt.%WC composite powder. The ball milling was operated at 200 r/min with a ball to powder ratio of 10:1. Meanwhile, stearic acid was used as a stabilizer to prevent the mixed powder from cold welding.

Table 2 Chemical composition of Ni60 alloy powder (wt.%)

Ni	Cr	B	Si	Fe	C
Bal.	14−19	3.0−4.5	3.5−5.0	<8.0	0.5−1.0

2.2 Fabrication of Ni−WC coating

The layer cladding equipment is a 1064 nm Nd:YAG solid-state fiber coupling output laser (JHL-GX-2000 laser processing machine) produced by Wuhan Chutian Company (China). The AlSi5Cu1Mg substrate was tilted by about 30°, as shown in Fig. 1.

The Ni−WC coating was placed on the surface of the AlSi5Cu1Mg by the preset powder method.

Ni60+20wt.%WC powder and 1 vol.% polyvinyl alcohol (PVA-124) solution were mixed into a paste and uniformly coated on the surface of AlSi5Cu1Mg. The AlSi5Cu1Mg was placed into a vacuum drying chamber to dry Ni60+20wt.%WC composite powder at 90 °C. The laser cladding experiment was carried out by adjusting scanning speeds. The technological parameters of the laser cladding are given in Table 3.

2.3 Characterization

Microstructure and elementary composition of the samples were analyzed by scanning electron microscopy (SEM, quanta-200) with EDS. X-ray diffraction (XRD) was used to study the phase composition of the cladding coating. The X-ray diffractometer was operated at 35 kV and 200 mA with nickel-filtered Cu K_α radiation as an incident beam (D/max 2550VL/PC). The microhardness was tested by the Victorinox (HXS-1000A) tester. The preload was set to be 100 N, and the preload time was 15 s. The microhardness of the cladding coating was tested along the vertical section from the surface to the bottom. The test interval was 100 μm each time. Three data were repeatedly tested at each point.

2.4 Electrochemical measurements

The corrosion resistance of the samples was estimated by the electrochemical measurements. The samples for the test were cut into rectangles in size of 10 mm × 10 mm × 3 mm. Prior to the tests, the samples were encapsulated in epoxy resin, ground to 2000 mesh sandpaper, cleaned with ethanol, and finally dried in air. The electrochemical tests were employed by a Princeton applied research (PARSTAT 4000) and a traditional three-electrode system. The working electrode was the sample with an effective exposure area of 1 cm^2. The counter electrode and the reference electrode were a platinum electrode and a silver/silver chloride electrode (Ag/AgCl in 3 mol/L KCl), respectively. The Tafel polarization curves were obtained at a scanning rate of 1 mV/s in the range of ±350 mV in 0.1 mol/L HCl solution at room temperature. The electrochemical impedance spectroscopy (EIS) measurements were performed in the frequency range from 100 kHz to 10 MHz. The linear scan voltammetry curve was analyzed by matching analysis software (VersaStudio software, P/N 224181). All the electrochemical test results are presented as the mean values of six measurements.

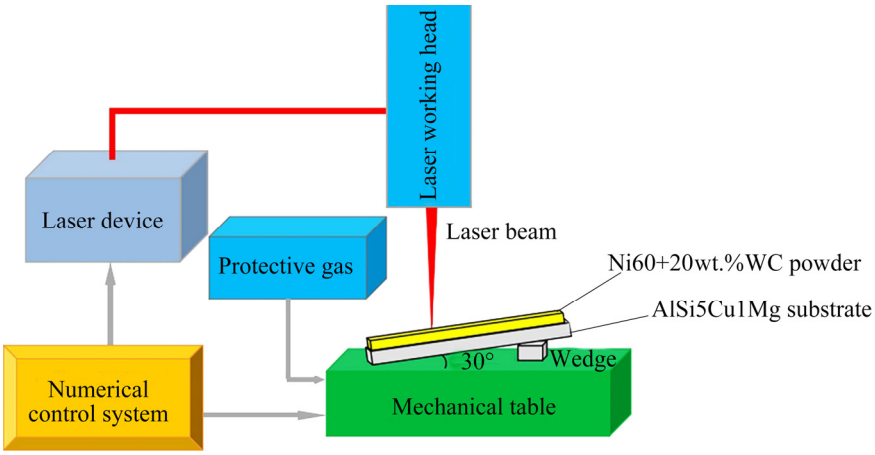

Fig. 1 Schematic diagram of laser cladding processing

Table 3 Technological parameters of laser cladding

Sample No.	Powder−bed depth/mm	Power/kW	Scanning speed/(mm·min^{-1})	Laser beam/mm	Flow rate of shield gas (Ar)/(L·min^{-1})
1	1.0	1.2	150	2.0	25
2	1.0	1.2	200	2.0	25
3	1.0	1.2	250	2.0	25
4	1.0	1.2	300	2.0	25

2.5 Immersion test

For the immersion test, the Ni−WC coating was immersed in 0.1 mol/L HCl solution for 5 days. Before the immersion, the samples were successively polished to 1000 mesh sandpaper followed by ultrasonic cleaning with ethanol solution for 5 min.

2.6 Calculation of dilution

In the laser cladding process, low dilution was pursued on the premise of ensuring good metallurgical bonding of the interface. The geometric method is used for the dilution calculation. The model is shown in Fig. 2, and the expression is as follows [26]:

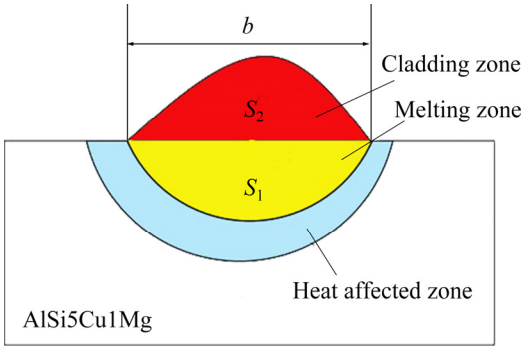

Fig. 2 Schematic diagram of single track geometrical measure

$$\lambda = \frac{S_1}{S_1 + S_2} \quad (1)$$

where λ is dilution rate; S_1 is melting zone area; S_2 is cladding zone area.

3 Results and discussion

3.1 Micromorphology of Ni−WC coating

Figure 3 shows cross-sectional morphologies of the Ni−WC coating at different scanning speeds. The surface quality of the laser cladding is influenced by scanning speed. With increasing scanning speed, the thickness of the cladding coating increases first and then decreases, while the width of the molten pool decreases throughout. The cladding layer size and dilution rate at different scanning speeds are given in Table 4.

As seen in Fig. 3(a), the coating is thin and the WC particles evenly distribute in the upper cladding coating at a scanning speed of 150 mm/min. However, a large number of cracks are generated at the edge of the coating. The dilution rate is 46%. The strong convection in the molten pool generated by the high laser energy enables homogeneous distribution of WC particles. Furthermore, the greater the temperature gradient is, the more easily the surface cracks occur. In Fig. 3(b), when the

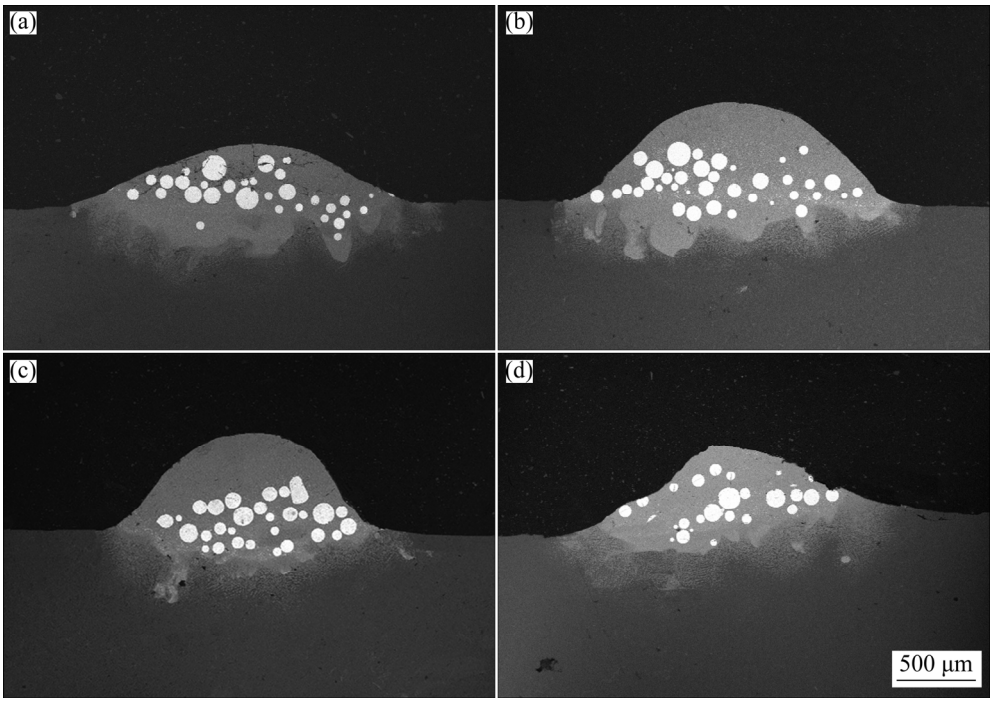

Fig. 3 Cross-sectional morphologies of Ni−WC coating at different scanning speeds: (a) 150 mm/min; (b) 200 mm/min; (c) 250 mm/min; (d) 300 mm/min

Table 4 Cladding layer size and dilution rate of Ni−WC coating at different scanning speeds

Scanning speed/ (mm·min^{-1})	Melting zone area, S_1/μm^2	Cladding area, S_2/μm^2	Welding pool width/ μm	Dilution rate/%
150	47567	55318	2167	46
200	30988	75808	2105	29
250	25715	79287	1861	24
300	13812	46871	1825	22

scanning speed increases to 200 mm/min, the dilution rate is 29%. Obviously, the WC particles distribute in the middle of cladding coating, and the cracks are restrained. With increasing the scanning speed, the heating time of the molten pool is shorter and the temperature gradient and thermal stress are smaller, so the cracks are reduced. Meanwhile, the coating prepared at scanning speed of 200 mm/min has better metallurgical bonding than that prepared at 150 mm/min. However, the distribution of WC particles is not uniform with some agglomeration. As shown in Fig. 3(c), the WC particles evenly distribute in the middle and bottom of the cladding coating and the surface is smooth with no obvious cracks at a scanning speed of 250 mm/min. Meanwhile, the dilution rate is relatively low at 24% and the metallurgical bonding is excellent. In Fig. 3(d), when the scanning speed further increases to 300 mm/min, the dilution ratio is further reduced to 22%. Although the dilution rate is minimal, the cladding coating surface is very rough and the thickness is very small, which indicates that composite powder is not heated enough to completely melt at the high scanning speed and cannot produce a good metallurgical bond.

From the above, the optimum scanning speed is chosen to be 250 mm/min, in which the cladding coating displays smooth micromorphology without obvious cracks and the WC particles uniformly distribute in the cladding coating with low dilution rate. The fine microstructure and homogeneous distribution of WC particles in the cladding coating are influenced by the effect of melt convection and gravity. The viscosity and surface tension of the mixed melt at the top of the layer are higher than those of the alloy melt at the bottom. According to the Marangoni effect [27], the Al alloy melt continuously penetrates the WC/Ni mixed melt, forming convection inside the melt. The convection model of the WC/Ni mixed melt pool is shown in Fig. 4. At high temperature, under the influence of convection, WC particles are uniformly distributed and suspended in the melt on cladding. Meanwhile, the density of WC particles (16.5 g/cm^3) is much higher than that of bonding metal Ni (7.53 g/cm^3). Therefore, due to the gravity, a portion of WC particles moves to the bottom of the layer. Based on the above reasons, most WC particles accumulate on the solidified interface of the layer.

3.2 Microstructure and composition of Ni−WC coating

Figure 5(a) shows the SEM images of cladding coating at a scanning rate of 250 mm/min. It can be observed that WC particles disperse in the middle of the cladding coating and there are fine white phases around the WC particles. The morphology and EDS spectrum of fine white phases are shown in Figs. 5(a) and 5(b), respectively. The fine white phases are mainly composed of C, Ni, Al, Cr, W and Fe elements. It can be seen that the fine white phases are composite carbide generated by Al matrix and Ni60+20wt.%WC composite powder under the laser action. The following crystalline phase transformations occur [28,29]:

$$L \rightarrow M_7C_3+M_{23}C_6 \ (M=Ni, Al, Cr, W, Fe) \quad (2)$$

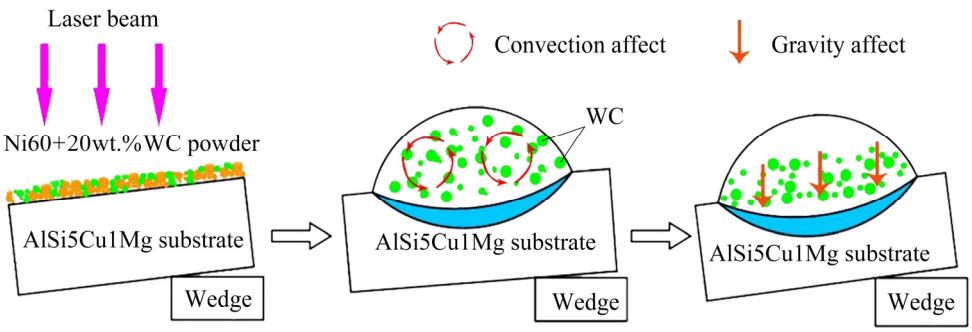

Fig. 4 Schematic diagram of distribution model of WC particles

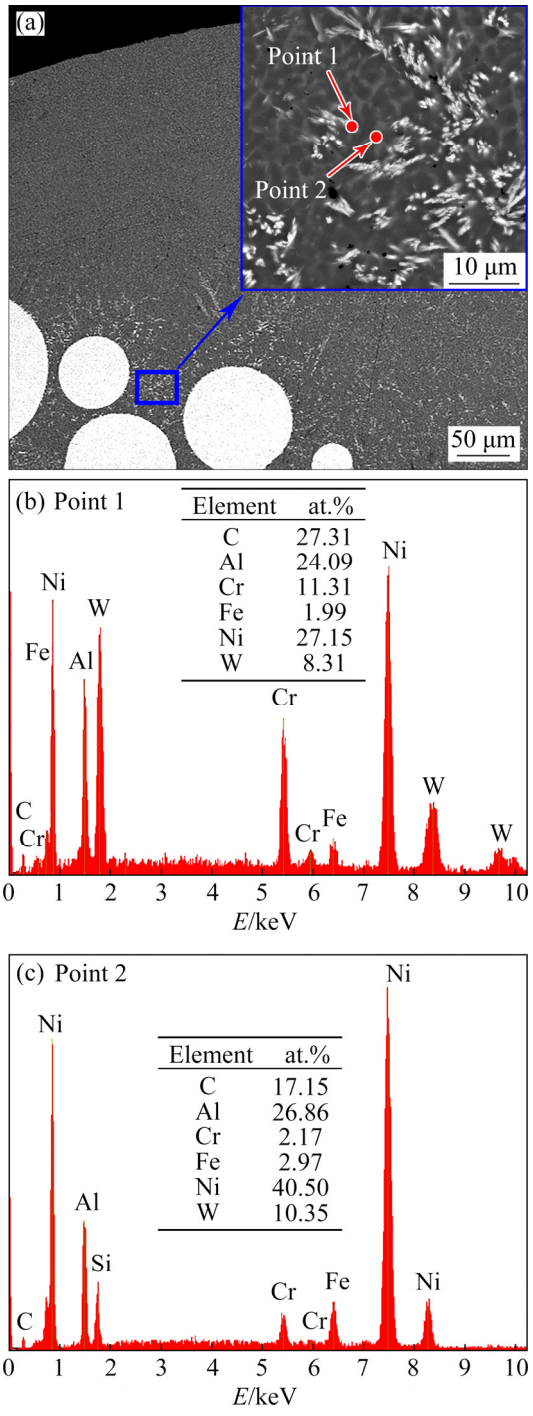

Fig. 5 SEM image (a) and EDS spectra (b, c) of cladding coating at scanning rate of 250 mm/min

The formation mechanism of composite carbide is analyzed as follows. EDS analysis results show that WC particles are partially melted under the thermal effects of laser cladding. The free atoms of C and W in the Ni-based alloy can dissolve and diffuse into the molten pool, react with other elements, and promote the formation of mixed carbides during solidification. According to the solidification theory of metals, the complicated reaction of carbides in the molten pool can take place as follows [30]:

$$L+WC\rightarrow W_2C \quad (3)$$

$$L+(Cr,Fe)_2C\rightarrow(Cr,Fe)_7C_3 \quad (4)$$

$$L+(Cr,Fe)C\rightarrow(Cr,Fe)_{23}C_6 \quad (5)$$

The image in Fig. 5(a) shows that carbides preferentially nucleate at the boundary of undissolved WC particles, and thus the carbides are formed in a dendrite and acicular pattern. The dendrite and acicular carbides with fine size are formed by component supercooling in the cladding coating and melt convection in the molten pool. Using Ni60+WC powder coating on the Q550 steel substrate, MA et al [30] synthesized the same carbides (M_7C_3 and $M_{23}C_6$) using a laser cladding process, whose morphologies are similar as the fine white phase.

As shown in Fig. 5(a), there are also some reticulated gray phases in the cladding coating. The reticulated gray phases distribute throughout the whole cladding coating. The EDS scanning of the gray phase was performed and the result is shown in Fig. 5(c). The reticulated gray phases primarily consist of Ni, Al, C, Si, Cr and Fe elements. Under the action of the laser, the Al substrate and Ni60 show the following chemical reactions by melt convection [31−33]:

$$Ni+Al=NiAl \quad (6)$$

$$3Ni+Al=Ni_3Al \quad (7)$$

$$2Ni+NiAl=Ni_3Al \quad (8)$$

The Gibbs free energy values of the above three reactions at 1200 °C are −96.51, −127.36 and −30.85 kJ/mol, respectively. The negative Gibbs free energy values indicate that all of the reactions can be carried out thermodynamically. In the reaction process, the NiAl phase is formed prior to the Ni_3Al phase. The NiAl phase grows into fine equiaxed crystal, and the Ni_3Al phase grows into a network structure around the NiAl phase.

To further confirm the phase composition of the cladding coating, XRD analysis was carried out and the result is shown in Fig. 6. The strong diffraction peaks of NiAl and Ni_3Al phases can be seen in the pattern, which represent the typical chemical reactions by melt convection between Al and Ni60. In the meantime, typical characteristic

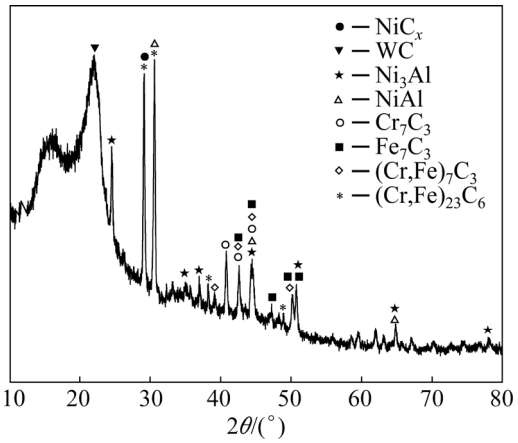

Fig. 6 XRD pattern of cladding coating

peaks of Cr_7C_3, Fe_7C_3, $(Cr,Fe)_7C_3$ and $(Fe,Ni)_{23}C_6$ phases are detected, which confirms the crystalline phase transformations. By combining the results of EDS and XRD, it is concluded that NiAl, Ni_3Al, M_7C_3, $M_{23}C_3$ (M=Cr, Fe, Al) and other carbon compounds are formed in the cladding coating. It can be seen that the pattern contains some diffraction peaks of WC, which represent the WC particles in the coating.

Figure 7 shows BSE images and corresponding EDS map scanning results of WC particle of cladding coating at a scanning rate of 250 mm/min. Notably, elemental diffusion occurs between WC particles and Ni-based binder in the cladding coating. Cr and Fe diffuse into WC particles, and C diffuses into the Ni-based binder. Meanwhile, irregular white phases exist at the bonding interface, Cr is clustered, and this phenomenon is consistent with the aggregation of Cr at the bonding interface. The elemental diffusion phenomenon proves that a good metallurgical bond is formed between WC particles and the Ni-based binder.

Figure 8 shows the SEM images of the heat-affected zone at a scanning rate of 250 mm/min and the EDS analysis results of Points 1 and 2. The morphology of the heat-affected zone changes from cellular crystal to dendritic crystal. The dilution effect of Al in the binding zone is obvious. According to the EDS analysis of Point 1, the content of Al in the cellular zone is 32.12 at.%, while the contents of C and Ni in the dendritic zone are 13.63 and 13.01 at.%, respectively, for Point 2. The elemental diffusion phenomenon of the heat-affected zone proves that a good metallurgical bond is formed between cladding coating and AlSi5Cu1Mg.

3.3 Microhardness of Ni−WC coating

The microhardness values of the Ni−WC coating prepared at a scanning rate of 250 mm/min and AlSi5Cu1Mg substrate are shown in Fig. 9.

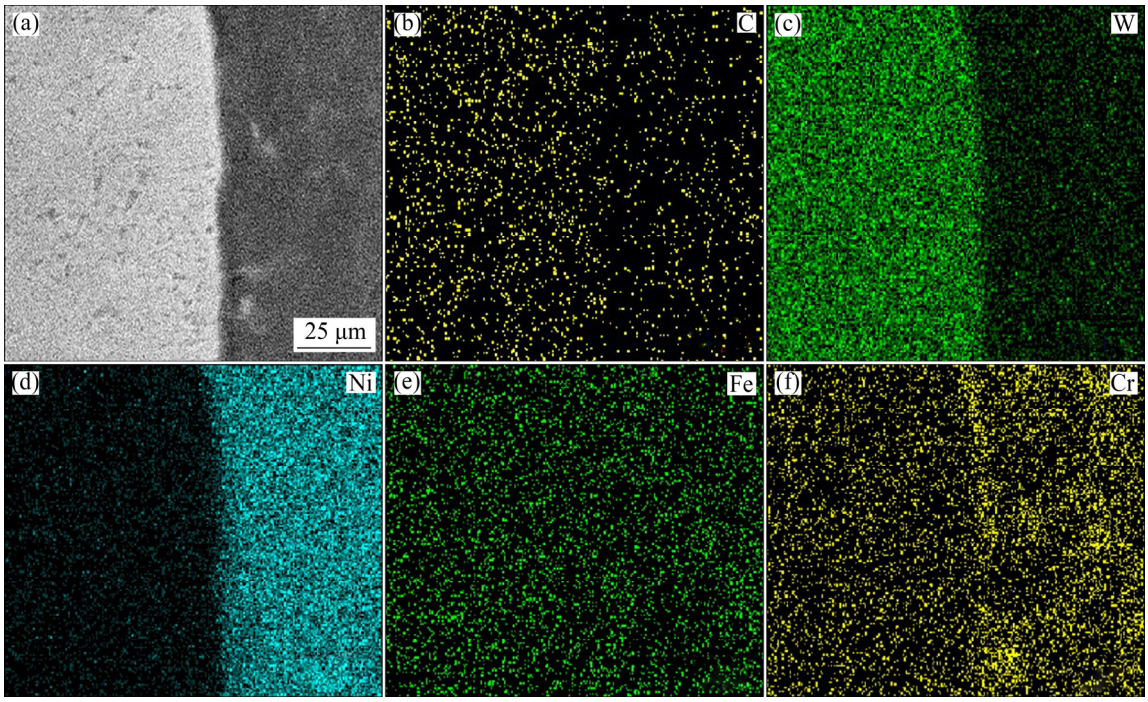

Fig. 7 BSE images of WC particle of cladding coating at scanning rate of 250 mm/min (a) and results of EDS map scanning (b−f)

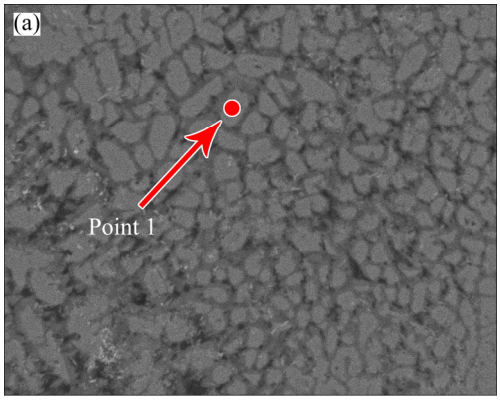

Element	Al	Ni	Cr	C	Others
at.%	32.12	37.34	3.67	15.82	11.05

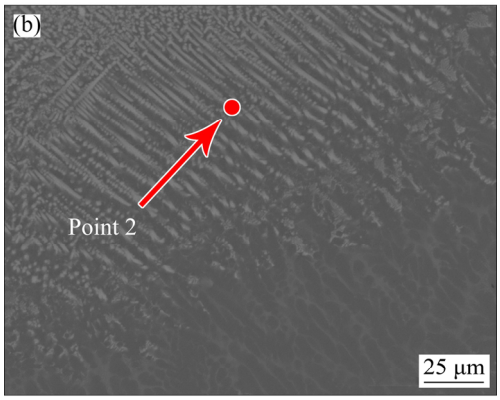

Element	Al	Ni	Cr	C	Others
at.%	65.85	13.01	0.35	13.63	7.16

Fig. 8 SEM images of heat-affected zone at scanning rate of 250 mm/min and EDS analysis results: (a) Point 1; (b) Point 2

In the cladding zone, the microhardness is relatively stable at a value of HV 680. In the melting zone, the microhardness increases first and then decreases, and reaches a maximum value of HV 925.1 at 500 μm away from the cladding surface, which is nearly 11 times that of AlSi5Cu1Mg substrate (HV 79). Then, the microhardness sharply decreases in the heat- affected zone and reaches a minimum value at AlSi5Cu1Mg. There are a large number of highly refined NiAl and Ni_3Al phases on the top of the cladding layer, which enables the microhardness of the cladding zone to reach a high value. More grain boundaries are introduced by grain refinement, which prevents the dislocation from moving among grains and enables the coating to be refined and strengthened. The maximum hardness observed in the middle of the melting zone is attributed to homogeneous distribution of WC particles and newly formed hard precipitated carbides (M_7C_3 and $M_{23}C_6$). The residual, uniformly distributed WC particles and fine carbides in the cladding coating play a role in dispersion strengthening to improve the microhardness. Meanwhile, Cr, W, Fe, Si and other elements are dissolved in the melt, which can provide more lattice distortion to hinder the dislocation movement. The coating becomes solution-strengthened, which improves the microhardness. Then, the microhardness of the melt zone decreases near the heated zone. The microhardness sharply decreasing in the heat- affected zone is attributed to the higher dilution effect of the Al substrate. Meanwhile, the grain morphology of the heat-affected zone is changed from large cellular crystal to slender dendritic crystal, and the slender dendritic crystal interacts with the matrix, which results in a decrease in microhardness of the heat-affected zone.

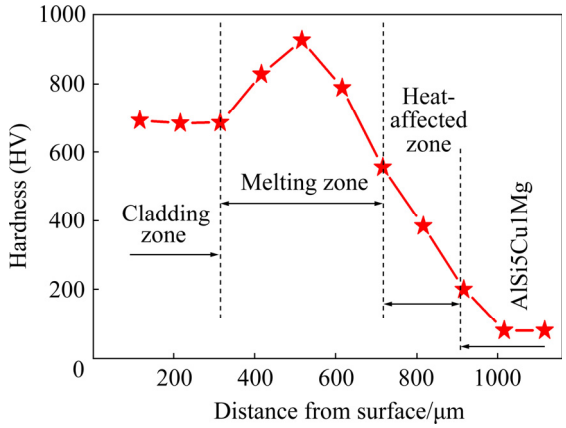

Fig. 9 Microhardness distribution of cladding coating on AlSi5Cu1Mg surface

3.4 Corrosion behavior of Ni−WC coating

3.4.1 Electrochemical properties

Figure 10(a) displays the potentiodynamic polarization curves of the cladding coating and AlSi5Cu1Mg in 0.1 mol/L HCl solution. Meanwhile, the corrosion potential (φ_{corr}) and corrosion current density (J_{corr}) were estimated via the potentiodynamic polarization curves. As seen in Fig. 10(a), the J_{corr} values of the cladding coating and AlSi5Cu1Mg are 12.33 and 58.79 μA/cm^2, respectively. The former is only 20.97% of the latter. The corrosion potential (φ_{corr}) is usually employed to describe the stability of the film on the surface of metal. φ_{corr} of the cladding coating is −318.09 mV, which is greater than that of AlSi5Cu1Mg (−627.89 mV). The smaller the corrosion current

density is, the better the corrosion resistance of the alloy is. The cladding coating exhibits higher φ_{corr} and lower J_{corr}, indicating enhanced corrosion resistance compared with AlSi5Cu1Mg.

Figures 10(b, c) show the Nyquist plots and Bode plots of cladding coating and AlSi5Cu1Mg, respectively. In the Nyquist plots, the radius of the impedance spectrum of cladding coating is larger than that of AlSi5Cu1Mg. Obviously, Fig. 10(c) shows that the impedance modulus of AlSi5Cu1Mg is less than that of cladding coating.

Figure 10(d) shows the equivalent circuit model of AlSi5Cu1Mg and cladding coating. R_1 represents the solution resistance, R_2 represents a thin film resistance dependent on passive film and composite coating, and CPE_1 represents the constant phase element of the film. The properties of CPE_1 are related to the value of CPE_1-T and CPE_1-P, as given in Table 5. The value of CPE_1-P is close to 0 or 1, representing that CPE_1 tends to be an ideal resistor or ideal capacitor, respectively [34]. The result of this equivalent circuit model fits the measured value very well because the Chi-squared values are less than 0.01. The R_2 value of the Ni−WC coating (1892.0 Ω·cm^2) is about 11 times that of AlSi5Cu1Mg (167.6 Ω·cm^2).

3.4.2 Immersion test results

The surface morphologies of the Ni−WC coating on AlSi5Cu1Mg after immersion in 0.1 mol/L HCl solution for 5 days are shown in Fig. 11. Obviously, different regions display different corrosion phenomena. The observed surface morphology after immersion shows that the cladding coating displays better corrosion resistance than AlSi5Cu1Mg.

From Fig. 11(a), the corroded surface of the

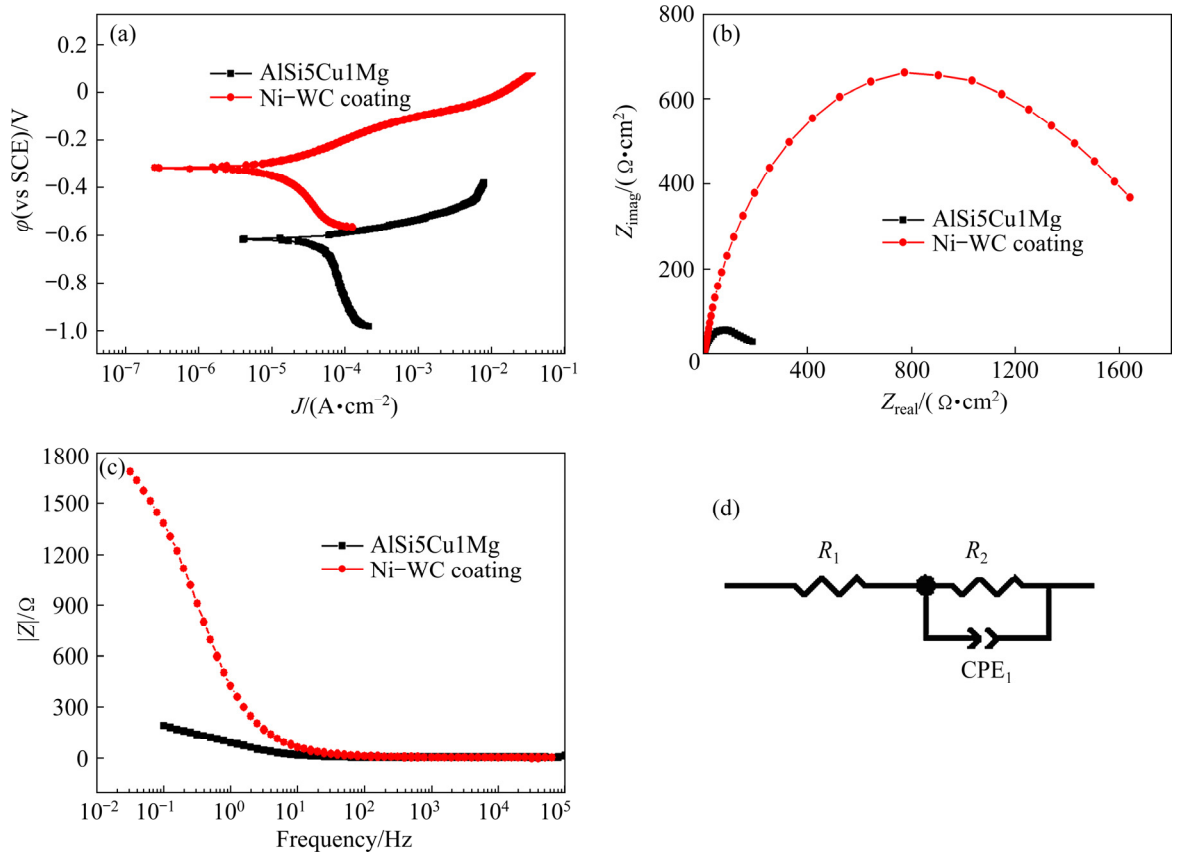

Fig. 10 Potentiodynamic polarization curves (a), Nyquist plots (b), Bode plots (c), and equivalent electrical circuit of metal/solution interface (d) of cladding coating and AlSi5Cu1Mg in 0.1 mol/L HCl solution

Table 5 Simulated parameters of EIS data for AlSi5Cu1Mg and Ni−WC coating

Material	R_1/(Ω·cm^2)	R_2/(Ω·cm^2)	CPE_1-T/(μF·s^P·cm^{-2})	CPE_1-P	Chi-squared value
AlSi5Cu1Mg	5.201	167.6	5.51×10^{-4}	0.831	1.09×10^{-3}
Ni−WC coating	3.004	1892.0	2.53×10^{-4}	0.796	1.97×10^{-3}

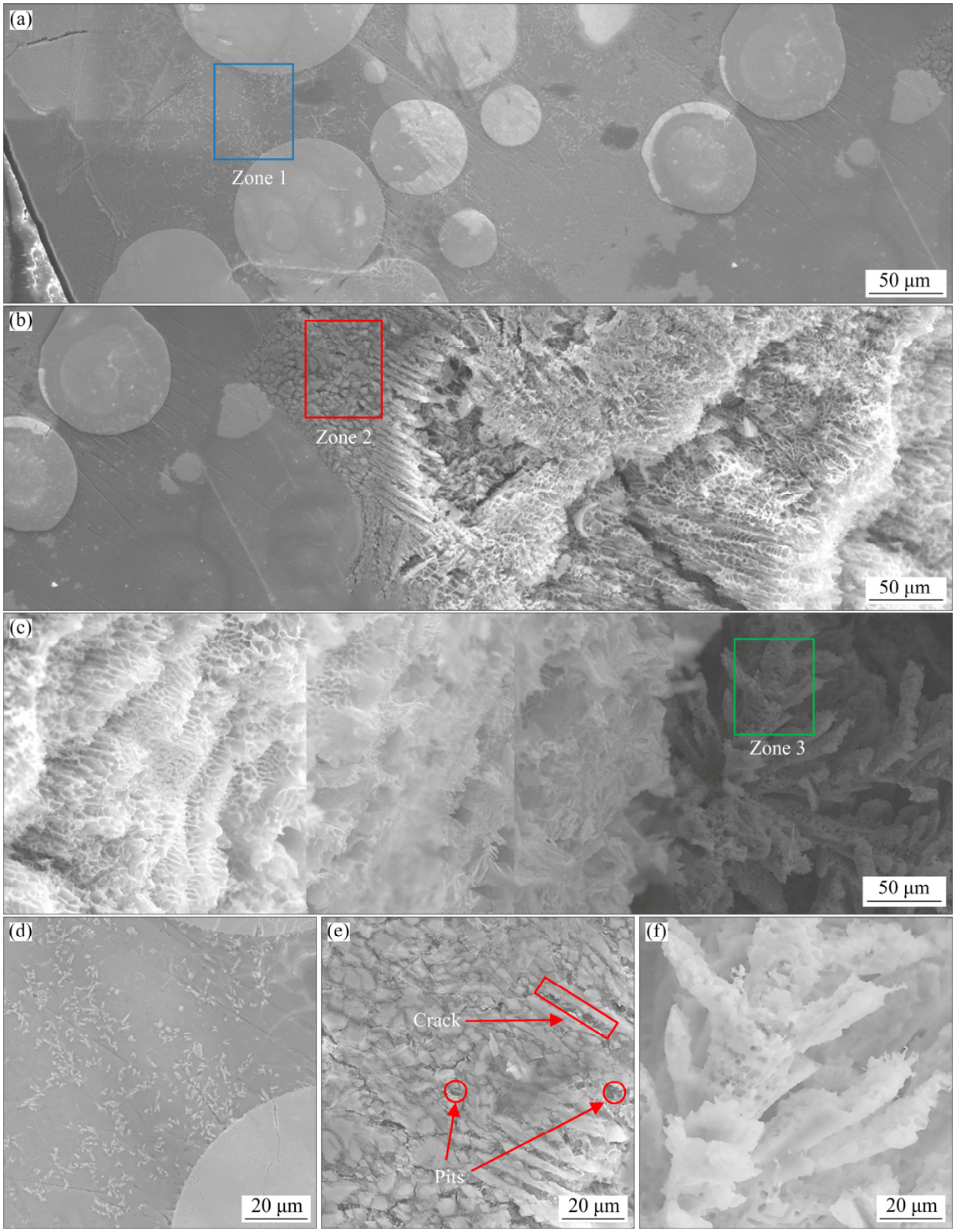

Fig. 11 SEM images of corrosion morphologies of cladding coating on AlSi5Cu1Mg: (a) Cladding zone and melt zone; (b) Melt zone and heat-affected zone; (c) Heat-affected zone and substrate; (d) Magnified image of Zone 1; (e) Magnified image of Zone 2; (f) Magnified image of Zone 3

cladding zone is relatively smooth with negligible variation after corroding treatment. No obvious corrosion pit is found from the high magnification of Zone 1, as shown in Fig. 11(d). The corrosion mechanism of the cladding coating is shown in Fig. 12(a). Firstly, the strong convection in the molten pool and rapid solidification during the laser cladding process result in a uniform distribution of WC particles and a gain refinement of the Ni-based equiaxial crystal. The cladding coating has fewer

cracks and pores, and the structure is homogeneous and compact, which can effectively inhibit erosion action of Cl^- ions and H^+ ions. Secondly, the M_7C_3 and $M_{23}C_6$ secondary carbides formed surrounding the WC particles act as a physical skeleton to protect the Ni-based binder from the preferential corrosive attack [25].

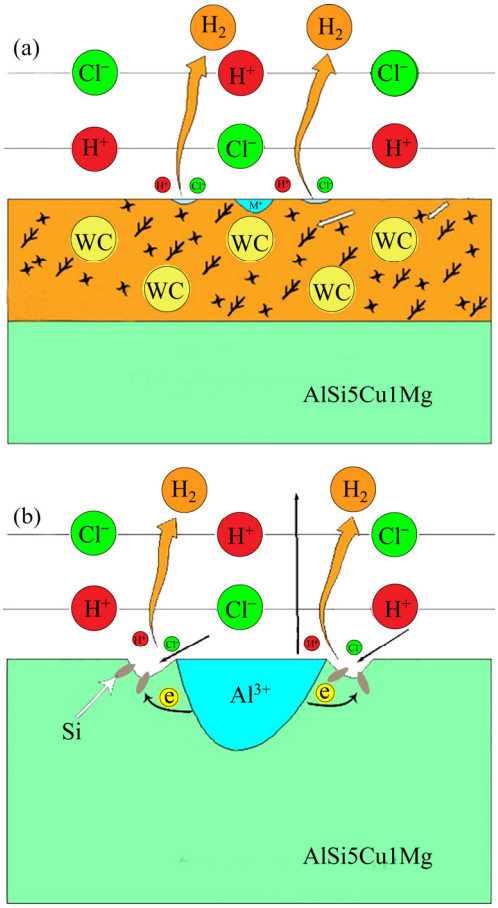

Fig. 12 Schematic diagram of different corrosion mechanisms: (a) Cladding coating; (b) AlSi5Cu1Mg

In Fig. 11(b), compared with the cladding zone, great changes take place on the surface of the heat-affected zone. A large number of corrosion pits, corrosion cracks, and peeling layers can be observed from the high magnification of Zone 2, as shown in Fig. 11(e). As the morphology of the heat-affected zone changes from cellular crystal to dendritic crystal, the size of the corrosion pit gradually grows, the number of peeling layers dramatically increases, and a defect appears in the substrate.

When the corrosion solution touches AlSi5Cu1Mg, the corrosion area and etching depth of AlSi5Cu1Mg surface remarkably increase, as shown in Fig. 11(c). AlSi5Cu1Mg is corroded seriously, the surface with a certain thickness is corroded away and only the fishbone silicon can be seen, as shown in Fig. 11(f). According to the surface morphology after immersion, the corrosion behavior is shown in Fig. 12(b). AlSi5Cu1Mg is seriously corroded and α(Al) is removed from the surface, where the corrosion for AlSi5Cu1Mg may be due to the micro galvanic corrosion between the phases in AlSi5Cu1Mg. In the microgalvanic corrosion depicted at the surface of AlSi5Cu1Mg, α(Al) acts as an anode, and the eutectic Si around it acts as a cathode. The corrosion reaction occurs on the surface of the Al−Si−Cu alloy:

$$\text{Anodic reaction: } Al-3e=Al^{3+} \quad (9)$$

$$\text{Cathodic reaction: } 2H^++2e=H_2\uparrow \quad (10)$$

$$\text{Overall reaction: } 2Al+6H^+=2Al^{3+}+3H_2\uparrow \quad (11)$$

This phenomenon is mainly due to the potential difference among various phases in the Al−Si−Cu alloy, and the corrosion behavior always initiates at α(Al) matrix in the adjacent areas of the eutectic Si, AlFeMnSi phase and Cu-rich phase [35]. Thus, AlSi5Cu1Mg exhibits an active anodic dissolution behavior and α(Al) corrodes quickly. The observed surface morphology after immersion testing shows that the Ni−WC coating displays better corrosion resistance than AlSi5Cu1Mg.

4 Conclusions

(1) Cladding coating with an optimum scanning rate of 250 mm/min produces a smooth surface without obvious cracks and the distribution of WC particles is homogeneous. The main phases of the cladding coating include NiAl, Ni_3Al, carbides (M_7C_3 and $M_{23}C_6$) and WC particles. Uniform distribution of the main phases is attributed to the strong melt convection effect caused by laser cladding.

(2) The microhardness of the cladding coating is HV 788.2−925.1, which is 9−11 times that of AlSi5Cu1Mg (HV 79). The better mechanical properties may be attributed to the newly formed carbides (M_7C_3 and $M_{23}C_6$) and the excellent metallurgical bond between cladding coating and AlSi5Cu1Mg.

(3) The cladding coating displays higher corrosion potential and lower corrosion current density (φ_{corr}=−318 mV and J_{corr}=12.33 μA/cm^2) than AlSi5Cu1Mg (φ_{corr}=−628 mV and J_{corr}=

58.79 μA/cm^2), which shows a larger corrosion resistance. Crack-free, dense, refined crystals of the cladding coating can inhibit the penetration of Cl^- and H^+, enabling the corrosion reaction difficult to occur.

References

[1] DINAHARAH I, MURUGAN N. Dry sliding wear behavior of AA6061/ZrB_2 in-situ composite [J]. Transactions of Nonferrous Metals Society of China, 2012, 22: 810−818.

[2] KARAKULAK E, ZERENR M, YAMANOLU R. Effect of heat treatment conditions on microstructure and wear behaviour of Al4Cu2Ni2Mg alloy [J]. Transactions of Nonferrous Metals Society of China, 2013, 23: 1898−1904.

[3] BENEA L, BONARA P L, BORELLO A, MARTELLI S. Wear corrosion properties of nano-structured SiC−nickel composite coatings obtained by electroplating [J]. Wear, 2001, 249: 995−1003.

[4] ESPALLARGAS N, BERGET J, GUILEMANY J M, BENEDETTI A V, SUEGAMA P H. Cr_3C_2−NiCr and WC−Ni thermal spray coatings as alternatives to hard chromium for erosion–corrosion resistance [J]. Surface & Coatings Technology, 2008, 202: 1405−1417.

[5] PRAVEEN A S, SARANGAN J, SURESH S, SIVA SUBRAMANIAN J. Erosion wear behaviour of plasma sprayed NiCrSiB/Al_2O_3 composite coating [J]. International Journal of Refractory Metals & Hard Materials, 2015, 52: 209−218.

[6] SANTA J F, BLANCO J A, GIRALDO J E, TORO A. Cavitation erosion of martensitic and austenitic stainless steel welded coatings [J]. Wear, 2011, 271: 1445−1453.

[7] ZAREZADEH MEHRIZI M, SHAMANIAN M, SAIDI A, SHOJA-RAZAZVI R, BEIGI R. Evaluation of oxidation behavior of laser clad CoWSi−WSi_2 coating on pure Ni substrate at different temperatures [J]. Ceramics International, 2015, 41: 9715−9721.

[8] ZHANG Peng-xiang, YAN Hong, SUN Yong-hui. Microstructure, microhardness and corrosion resistance of laser cladding Al_2O_3@Ni composite coating on 304 stainless steel [J]. Journal of Materials Science, 2021, 56: 1−16.

[9] LIU Xiu-bo, LIU Hai-qing, MENG Xiang-jun, SUN Cheng-feng, WANG Ming-di, QI Long-hao, SHI Gao-lian, WU Shao-hua. Effects of aging treatment on microstructure and tribological properties of nickel-based high-temperature self-lubrication wear resistant composite coatings by laser cladding [J]. Materials Chemistry & Physics, 2014, 143: 616−621.

[10] XIONG Ling-ling, ZHENG Hai-zhong, YU Ping, LI Gui-fa, CHEN Zheng, ZHANG Bin. Laser-clad YSZ@Ni (core−shell nanoparticle) composites coatings [J]. Ceramics International, 2015, 41: 13850−13854.

[11] VAEZI M R, SADRNEZHAAD S K, NIKZAD L. Electrodeposition of Ni–SiC nano-composite coatings and evaluation of wear and corrosion resistance and electroplating characteristics [J]. Colloids and Surfaces A−Physicochemical and Engineering Aspects, 2008, 315: 176−182.

[12] ZHONG Min-lin, LIU Wen-jin, ZHANG Yu, ZHU Xiao-feng. Formation of WC/Ni hard alloy coating by laser cladding of W/C/Ni pure element powder blend [J]. International Journal of Refractory Metals & Hard Materials, 2006, 24: 453−460.

[13] ZHANG Zhi-hui, WANG Xi, ZHANG Qing-quan, LIANG Yun-hong, LI Xiu-juan. Fabrication of Fe-based composite coatings reinforced by TiC particles and its microstructure and wear resistance of 40Cr gear steel by low energy pulsed laser cladding [J]. Optics and Laser Technology, 2019, 119: 105622.

[14] LIU Ai-guo, GUO Mian-huan, HU Hai-long, LI Zhi-jie. Microstructure of Cr_3C_2-reinforced surface metal matrix composite produced by gas tungsten arc melt injection [J]. Scripta Materialia, 2008, 59: 231−234.

[15] ZHOU Sheng-feng, HUANG Yong-jun, ZENG Xiao-yan, HU Qian-wu. Microstructure characteristics of Ni-based WC composite coatings by laser induction hybrid rapid cladding [J]. Materials Science and Engineering A−Structural Materials Properties Microstructure and Processing, 2008, 480: 564−572.

[16] HU Miao, TANG Jian-cheng, CHEN Xin-gui, YE Nan, ZHAO Xin-yue, XU Miao-miao. Microstructure and properties of WC−12Co composite coatings prepared by laser cladding [J]. Transactions of Nonferrous Metals Society of China, 2020, 30: 1017−1030.

[17] GUO Chun, ZHOU Jian-song, CHEN Jian-min, ZHAO Jie-rong, YU You-jun, ZHOU Hui-di. High temperature wear resistance of laser cladding NiCrBSi and NiCrBSi/WC−Ni composite coatings [J]. Wear, 2011, 270: 492−498.

[18] FERNANDEZ M R, GARCIA A, CUETOS J M, GONZALEZ R, NORIEGA A, CADENAS M. Effect of actual WC content on the reciprocating wear of a laser cladding NiCrBSi alloy reinforced with WC [J]. Wear, 2015, 324−235: 80−89.

[19] WENG Zhi-kun, WANG Ai-hua, WU Xu-hao, WANG Yu-ying, YANG Zhi-xiang. Wear resistance of diode laser-clad Ni/WC composite coatings at different temperatures [J]. Surface & Coating Technology, 2016, 304: 283−292.

[20] ZHOU Sheng-feng, LEI Jian-bo, DAI Xiao-qin, GUO Jin-bo, GU Zhen-jie, PAN Hong-bo. A comparative study of the structure and wear resistance of NiCrBSi/50wt.%WC composite coatings by laser cladding and laser induction hybrid cladding [J]. International Journal of Refractory Metals & Hard Materials, 2016, 60: 17−27.

[21] DONG Shi-yun, MA Yun-zhe, XU Bin. Current status of material for laser cladding [J]. Materials Review, 2006, 20: 8.

[22] SCHOLL H, HOFMAN B, RAUSCHER A. Anodic polarization of cemented carbides of the type [(WC, M): M = Fe, Ni or Co] in sulphuric acid solution [J]. Electrochimica Acta, 1992, 37: 447−452.

[23] CHO J E, HWANG S Y, KIM K Y. Corrosion behavior of thermal sprayed WC cermet coatings having various metallic binders in strong acidic environment [J]. Surface & Coatings Technology, 2006, 200: 2653−2662.

[24] HIDOUCI A, PELLETIER J M, DUCOIN F, DEZERT D, EL GUERJOUMA R. Microstructural and mechanical characteristics of laser coatings [J]. Surface & Coatings Technology, 2000, 123: 17−23.
[25] FARAHMAND P, KOVACEVIC R. Corrosion and wear behavior of laser cladded Ni−WC coatings [J]. Surface & Coatings Technology, 2015, 276: 121−135.
[26] HUANG Yong-jun. Characterization of dilution action in laser-induction hybrid cladding [J]. Optics Laser Technology, 2011, 43: 965−973.
[27] YANG Cheng-yuan, CHENG Xu, TANG Hai-bo, TIAN Xiang-jun, LIU Dong. Influence of microstructures and wear behaviors of the microalloyed coatings on TC11 alloy surface using laser cladding technique [J]. Surface & Coating Technology, 2018, 337: 97−103.
[28] LEMKEY F D, GUPTA H, NOWOTNY H H, WAYNE S F. Carbides in iron-rich Fe−Mn−Cr−Mo−Al−Si−C systems [J]. Journal of Materials Science, 1984, 19: 965−973.
[29] MAYER S, LEITNER H, SCHEU C, SILLER I, CLEMENS H. Changes in tempering and its effect on precipitation behaviour in a hot-work tool steel [J]. Steel Research International, 2009, 80: 89−959.
[30] MA Qu-shuang, LI Ya-jiang, WANG Juan, LIU Kun. Homogenization of carbides in Ni60/WC composite coatings made by fiber laser remelting [J]. Materials and Manufacturing Processes, 2015, 30: 1417−1424.
[31] VOLOVITCH P, MASSE J, FABRE A, BARRALLIER L, SAIKALY W. Microstructure and corrosion resistance of magnesium alloy ZE41 with laser surface cladding by Al−Si powder [J]. Surface & Coatings Technology, 2008, 202: 4901−4914.
[32] TSAO C L, CHEN S. Interfacial reactions in the liquid diffusion couples of Mg/Ni, Al/Ni and Al/(Ni)−Al_2O_3 systems [J]. Journal of Materials Science, 1995, 30: 5215−5222.
[33] KECSKES L J, SZEWCZYK S T, PEIKRISHVILI A B, CHIKHRADZE N M. Hot explosive compaction of aluminum-nickelide composites [J]. Metallurgical and Materials Transactions A−Physical metallurgy and Materials Science, 2004, 35: 1125−1131.
[34] ZOU Yong-cheng, YAN Hong, YU Bao-biao, HU Zhi. Effect of rare earth Yb on microstructure and corrosion resistance of ADC12 aluminum alloy [J]. Intermetallics, 2019, 110: 104687.
[35] ARRABAL R, MINGO B, PARDO A, MOHEDANO M, MERINO M C, RIVAS A. Microstructure and corrosion behaviour of A356 aluminum alloy modified with Nd [J]. Materials and Corrosion, 2015, 66: 535−541.

AlSi5Cu1Mg 表面激光熔覆 Ni−WC 涂层的显微组织、硬度和耐蚀性能

曾 敏[1,2,3]，闫 洪[1,2]，喻保标[1]，胡 志[1]

1. 南昌大学 机电工程学院，南昌 330031；
2. 南昌市轻合金材料制备与加工重点实验室，南昌 330031；
3. 南昌工学院 新能源车辆学院，南昌 330108

摘 要：通过 SEM、XRD、硬度测试、浸泡测试和电化学测试等方法研究 AlSi5Cu1Mg 合金表面激光熔覆 Ni−WC 涂层的显微组织、硬度和耐蚀性。结果表明，Ni−WC 涂层组织致密、表面光滑，涂层中存在大量的 NiAl、Ni_3Al、M_7C_3、$M_{23}C_6$ 相(M=Ni、Al、Cr、W、Fe)和 WC 颗粒。当激光扫描速度为 120 mm/min 时，在优异的冶金结合和新生成的碳化物协同作用下，Ni−WC 涂层的显微硬度明显提高，为基体 AlSi5Cu1Mg 合金的 9~11 倍；与基体相比，Ni−WC 涂层表现出较高的腐蚀电位(−318.09 mV)和较低的腐蚀电流密度(12.33 μA/cm^2)。无裂纹、致密的 Ni−WC 涂层能抑制 Cl^-和 H^+的渗透，耐蚀性得到大幅提高。

关键词：激光熔覆；Ni−WC 涂层；AlSi5Cu1Mg；力学性能；耐蚀性

(Edited by Bing YANG)